Pattern Design of Diffractive Optical Sensor Elements for Multiplex Interferometry

Johannes Bläsi, Richard De La Rue, *Life Fellow, IEEE*, and Martina Gerken, *Senior Member, IEEE*

***Abstract*— In interferometric optical sensors, phase information is extracted from the modulated light intensity. In the case of free-standing interferometers, operating through the far-field interferogram, multiplex phase detection is not trivial. Multipinhole or multimicrodisk interferometry are examples of common-path interferometers that allow multiplex interferometric phase detection. Thereby an unambiguous interference pattern is required, with no overlap of multiple spatial frequencies. A common pattern in multipinhole interferometry is a circular arrangement. To increase the element density of the pattern, Golomb rulers are an interesting concept. Golomb rulers and rectangles are known from sonar and radar applications. Recently, they were applied for encoding in quantum information systems. In this publication, we investigate different pattern designs of circular diffractors that produce unique spatial frequencies. We introduce design algorithms. The optimization criteria are the uniqueness of the spatial frequencies, which show no overlap with any other frequency, and the density of the microdisk pattern. Golomb patterns increase the element density by about 30% compared to the circular pattern. Depending on the pattern area, the density of the circular Archimedes spiral surpasses by up to 13% the density of a square Golomb pattern, referenced to a circular area. To validate the theoretically designed patterns, examples are fabricated on the basis of photonic crystal microdisk elements and are characterized optically.**

***Index Terms*— Golomb rectangles, interferometry, multiplexing, phase detection, photonic crystals.**

I. Introduction

INTERFEROMETRIC optical sensors are among the most sensitive measurement methods for refractive index sensing. A change in refractive index results in a phase shift of the light interacting with the refractive index medium. The phase information of a detection arm is measured relative to a reference arm. The superposition and interference of the two light waves result in a modulated light intensity. Usually, for waveguide integrated interferometers, Mach–Zehnder [1], [2], [3] or Young's [4], [5] configurations are used. The first is based on a Y-junction to separate the light waves into two arms, with another Y-junction for combining them. At its output, a photodiode can measure the change in light intensity. Young's interferometers do not have the second Y-junction. Instead, the different waveguide outputs interfere in the far field and form an interferogram that can be processed. Optical fiber-based interferometers rely on Fabry–Perot [6], [7], [8], fiber Bragg gratings [9], or Mach–Zehnder configurations [10], [11]. These are advantageous technologies for pressure, strain, temperature, and ultrasound sensing. Especially for medical imaging and structural health monitoring [12]. Also, nonwaveguide-based free-standing interferometers are common as sensing instruments. Examples of free-standing interferometers include Michelson, Mach–Zehnder [13], and common-path [14] configurations. Depending on the configuration, multiplexing is performed differently. Sensors based on integrated Mach–Zehnder interferometers can implement large multiples of these structures on a single chip [15]. Also, optical fiber sensors can be bundled for multiplexing [12], [16]. For hyperspectral imaging of the surface roughness with a single shot, a multiplex Michelson interferometer based on a pinhole and a microlens array was introduced [17]. In the case of Young's configuration, for integrated interferometers—but also for free-standing Young's or common-path interferometers [14]—multiplexing is not so easy. In particular, the outputs of the single interferometers should not interfere with each other. The spatial separation required reduces the compactness of the system. On the other hand, techniques such as multipinhole [18], [19], [20], [21], [22], and microdisk [23] interferometry have been introduced that allow the outputs of all arms or light paths to interfere with each other without losing information. Here, the key is to find a geometrical arrangement of the outputs that produce unique spatial frequencies for each pair of outputs. The unambiguous spatial frequency pattern shows no overlap of spatial frequencies. A common pattern in multipinhole interferometry is a circular arrangement [19], [24].

To increase the element density of the pattern, Golomb rulers are an interesting concept. Golomb rulers [25] and rectangles [26], [27], [28] are known from sonar and radar applications. Recently, they were applied for encoding in quantum information systems [29]. A Golomb rectangle is a 2-D array with ones and zeros. Its 2-D autocorrelation is allowed to have only three values: "0," "1," and "K," whereby K is the number of "1s" in the array. An optimum Golomb rectangle has the maximum number of "1s" for a given array size [26].

In this publication, we investigate different pattern designs for circular diffractor elements that produce unique spatial frequencies. For this investigation, microdisks [30] are used. Thereby the criteria for which the designs are optimized are the uniqueness of the spatial frequencies, which show no overlap

Manuscript received 3 March 2023; revised 13 June 2023; accepted 3 July 2023. Date of publication 14 July 2023; date of current version 7 August 2023. The Associate Editor coordinating the review process was Dr. Liuyang Zhang. *(Corresponding author: Johannes Bläsi.)*

Johannes Bläsi and Martina Gerken are with the Chair for Integrated Systems and Photonics, Institute of Electrical and Information Engineering Kiel University, 24143 Kiel, Germany (e-mail: jbl@tf.uni-kiel.de; mge@tf.uni-kiel.de).

Richard De La Rue is with the Optoelectronics Research Group, School of Engineering, University of Glasgow, G12 8LT Glasgow, U.K.

This article has supplementary downloadable material available at https://doi.org/10.1109/TIM.2023.3295470, provided by the authors.

Digital Object Identifier 10.1109/TIM.2023.3295470

with any other frequency, and the density of the microdisk pattern.

II. Methods

A. Multimicrodisk Interferometry

The pattern designs are to be used in our multiplex microdisk common-path interferometer [30] [see Fig. 1(b)]. The latter is used for the experimental far-field measurements described in Section III-H. The measurement setup uses collimated light from a He–Ne laser to excite the guided-mode resonance (GMR) in photonic crystal microdisks with an incident angle of 7°. The microdisks are fabricated on a glass substrate. The excitation light couples into the disks from the backside of the glass substrate. GMRs in photonic crystals exhibit strong reflection. Upon refractive index changes at the photonic crystal surface, a GMR wavelength and phase shift occurs, making it useful for sensing applications. The 150-μm diameter microdisks diffract the reflected GMR light. Fig. 1(b) shows the reflection part of the setup. To reduce the reflection at the glass–air interface of the glass substrate a circular polarization filter is placed into the light path of the incoming and reflecting light, suppressing the nonresonant reflection. A Fourier lens ($f = 150$ mm) projects the far-field onto a CMOS camera. A single microdisk diffracts the GMR light and forms an Airy disk. The first minimum is found at an angle $\theta_1 = 0.295°$ ($\sin\theta = 1.22\lambda/d$). Hence, the inner bright spot of the Airy disk has a diameter of 1544 μm at the Fourier lens. The Fourier lens collimates the light and projects it onto a camera in its back focal plane. The light beams from multiple microdisks will overlap and interfere with the back focal plane of the Fourier lens. In the case of two diffractive elements [see Fig. 1(a) (middle)], straight interference fringes are formed within the maximum of the Airy disk in the back focal plane. The fringe distance s depends on the focal length f and the distance d between the pair of microdisks: $s = f\lambda/d$. The spatial frequency of the interference fringes is shown in the Fourier domain of the far field [see Fig. 1(d) (middle)]. Its position in the Fourier domain is proportional to the difference vector of the two diffractive elements that produce the interference. The lowest row of images shows the effect of three diffractive elements. Each pair of two elements produce a spatial frequency in the far field. This results in a total of $N(N-1)$ frequencies when N elements are illuminated. Microdisk patterns have to be found that produce unambiguous and not overlapping spatial frequencies in the Fourier domain. The phase-difference information from each pair of microdisks can be computed from the complex value of its spatial frequency $f(u, v)$ in the Fourier domain [18], [19], [20]

$$f(u,v) = FT^{-1}\{I(X,Y)\} = \sum_{m=1}^{N}\sum_{n=1}^{N} P_{mn} A_m A_n e^{i(\phi_m - \phi_n)}. \quad (1)$$

It is proportional to the convolution P_{mn} of the mth with the nth diffractive element. Its phase is the phase difference between the two diffractive elements [19].

B. Far-Field Computation

For the validation of the designed patterns, the far-field intensity that is measured by a camera in the interferometric measurement setup is computed, as well as its spatial frequencies. To calculate the far-field diffraction pattern, Fourier optics are applied. The results of the process can be seen in [see Fig. 1(a), (c), and (d)]. The far-field [see Fig. 1(c)] is described by Fraunhofer diffraction theory. It is calculated by the 2-D Fourier transform of the field directly after interacting with the diffraction object [see Fig. 1(a)]. The spatial frequencies [see Fig. 1(d)] are obtained by another 2-D fast Fourier transform (FFT) of the far-field diffraction intensity. The dc component (middle bright spot) is filtered out in the Fourier domain. The computation is done with a MATLAB script described in the flowchart in Fig. 2. As input, the electric field behind the diffractive element is described by a matrix $M(m \times n)$. With m representing the x-coordinate and n the y-coordinate. All the pixels $M(m_{\mathrm{DE}}, n_{\mathrm{DE}})$ which represent the area of the diffractive element are set to "1." The rest of the matrix is "0." To include the phase φ, a phasor $\exp(i\varphi)$ is multiplied to the amplitude "1."

C. Finding a Pattern Design

The patterns have to be designed without overlapping spatial frequencies. Fig. 3 shows the importance of the uniqueness of the spatial frequencies. The microdisk pattern in Fig. 3(a) is designed to show in the Fourier domain a partial overlap of two spatial frequencies. The arrows indicate the difference vectors between a pair of elements. The positions of the spatial frequencies are determined by the difference vectors [18]. The effect of overlapping is observed in the magnitude [see Fig. 3(b) and (c)] and phase [see Fig. 3(d) and (e)]. Latter shows that the phase of the spatial frequency is the phase difference between the two elements producing the frequency. In the case of overlapping frequencies, the resulting phase is determined by the sum of complex numbers. Hence, it is influenced by the magnitudes and phases of the different frequencies. In this simple case, the phase could be retrieved. However, in more complex overlaps and experiments with real data, this gets difficult. Besides, the phase is extracted from the center region of the spatial frequency as the magnitude and hence the signal relative to the noise is the highest. Therefore, we focus on patterns without overlapping spatial frequencies.

To find such patterns, Section III introduces deterministic design approaches, such as circular and spiral designs, and iterative methods that develop the pattern according to a search algorithm. For the latter case, a similar algorithmic framework, described in the flowchart Fig. 4, is applied. The algorithm starts with a coordinate pair of the first element position. Afterward, a new potential coordinate pair is selected, according to a selection rule specific to different design methods (see Section III). Then a test for the pattern's frequency uniqueness is performed. For this purpose, all the locations of the spatial frequencies produced have to be calculated, which can be performed by computation of the far-field diffraction pattern (Fourier optics) of the test design and its FFT, as described in Section II-A. However, this is computationally intensive

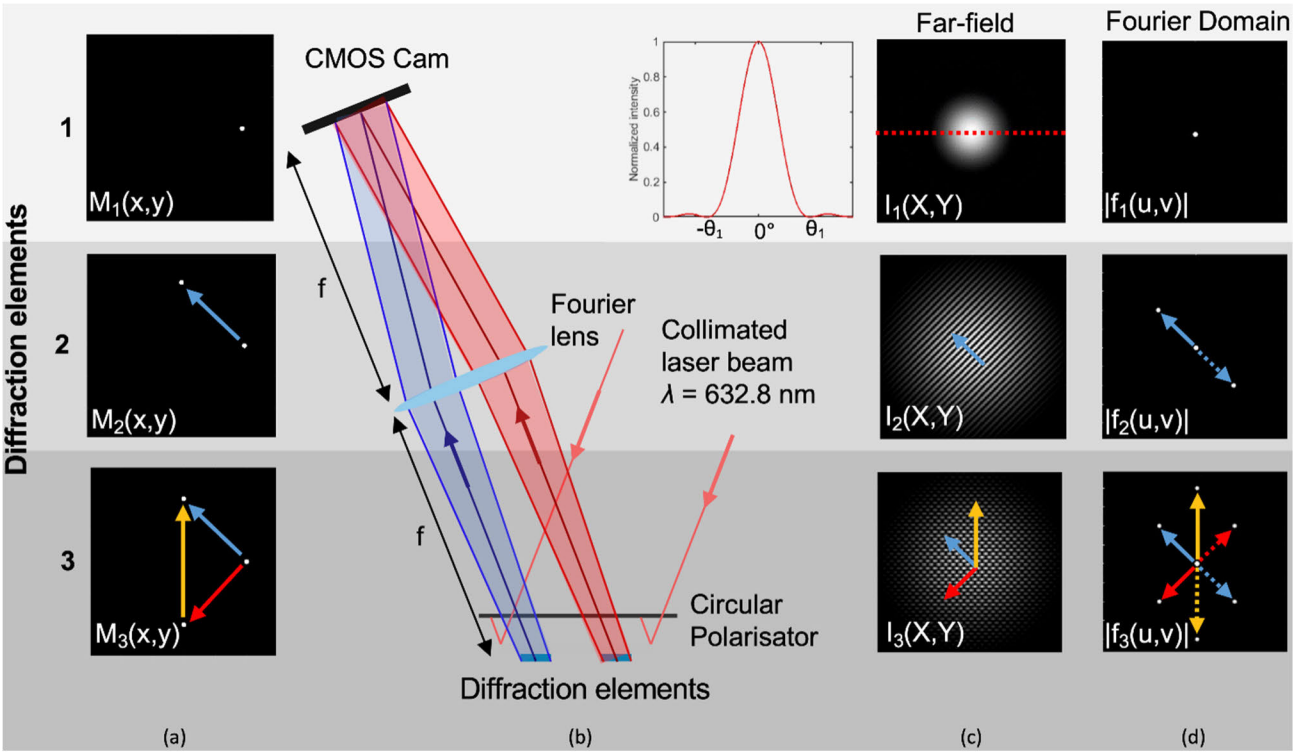

Fig. 1. Measurement setup and three simple element patterns. (a) Real-space microdisk distributions $M(x, y)$. (b) Optical setup showing the simplified reflection path with the diffraction elements, the Fourier lens, and the camera. (c) Intensity of far-field diffraction patterns $I(X, Y)$. (d) Magnitude $|f(u, v)|$ of the spatial frequencies $f(u, v)$ in the Fourier domain of the far-field intensity $I(X, Y)$.

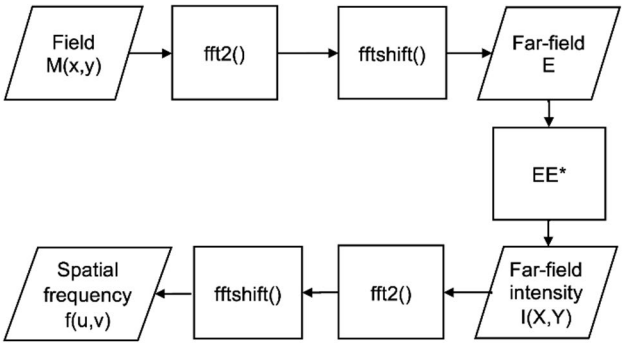

Fig. 2. MATLAB computation process of spatial frequency distribution based on input field matrix $M(x, y)$.

when we assume that an $N \times N$ matrix M represents the field distribution after the interaction with the diffractive element layer and its pixel resolution is 1 μm. In the case of a 7-mm wide field distribution, we would deal with a 7000 $\times$ 7000 matrix. In each iteration of the algorithm, this intensive computation would have to be performed. An alternative and more efficient approach is described in Section II-D. In the case of no overlap, the coordinate position is selected to place a diffractive element at this position. This process is repeated until the maximum number of elements is defined.

D. Test of Spatial Frequency Uniqueness

The computation of the far-field diffraction pattern and its spatial frequencies is very time-consuming when used in an iterative algorithmic framework (see Table I). A more efficient alternative is to use a lower resolution for the matrix describing the diffractive element positions. Thereby, each position in the matrix M describes the potential center position of one diffractive element. Matrix elements with a diffractive element are set to "1," otherwise to "0." By calculating the 2-D-autocorrelation in MATLAB of the matrix we obtain all the difference vectors which are positions of the spatial frequencies in the Fourier domain. Therefore, instead of using all pixels within one diffractive element, we reduce the element to its center position. Finally, based on the center positions, we can expand the matrix to a real-space matrix that has, within the radius around the center position of the diffractive element, all pixels set to one.

E. Element Density

To determine the density of the patterns, the number of elements is divided by the area that the pattern occupies. Since we are investigating circular- and square-shaped designs, the area is circular in the first case and square in the second case. Since we have a Gaussian laser beam in our setup and the laser spot exciting the elements in our patterns is circular, we also use, for some comparisons, a circular area for square-shaped patterns. This action reduced the density by comparison with a square area.

III. Results

In the following sections, different design approaches regarding the selection of the next coordinate are introduced

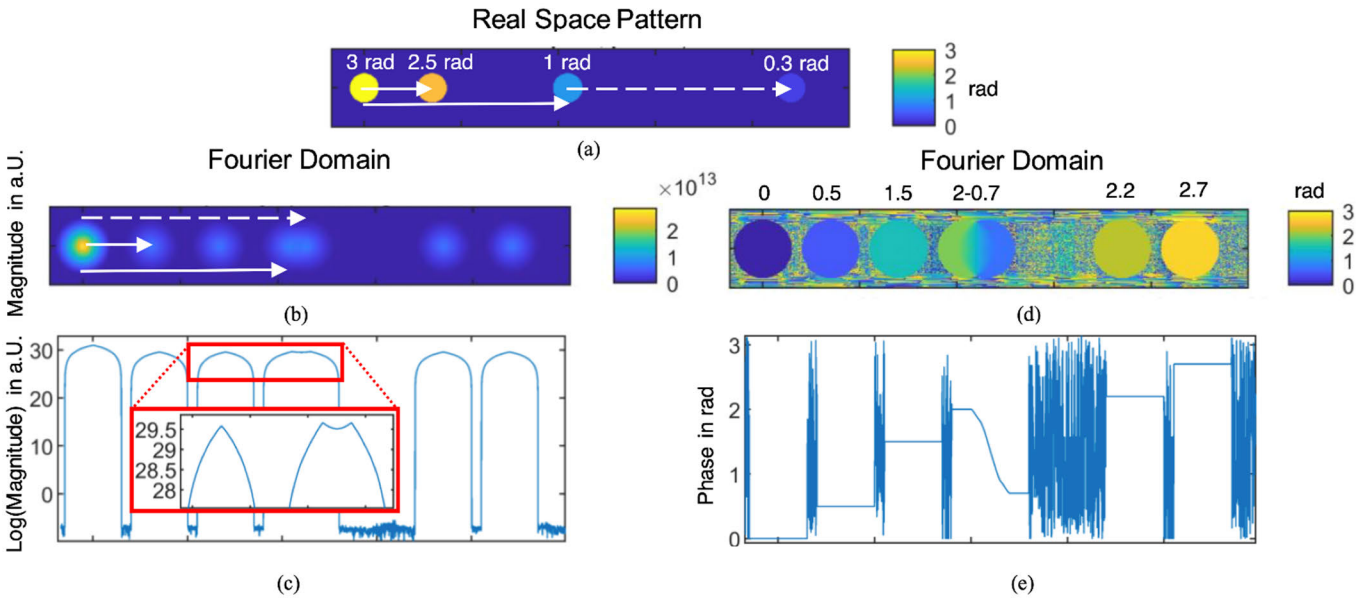

Fig. 3. Effect of overlapping spatial frequencies. (a) Microdisk pattern in real space with different phases. The arrows indicate the difference vectors of the elements. (b) Magnitude of the spatial frequencies in the Fourier domain. (c) Intersection plot of magnitude in log scale. (d) Corresponding phase and (e) its intersection plot.

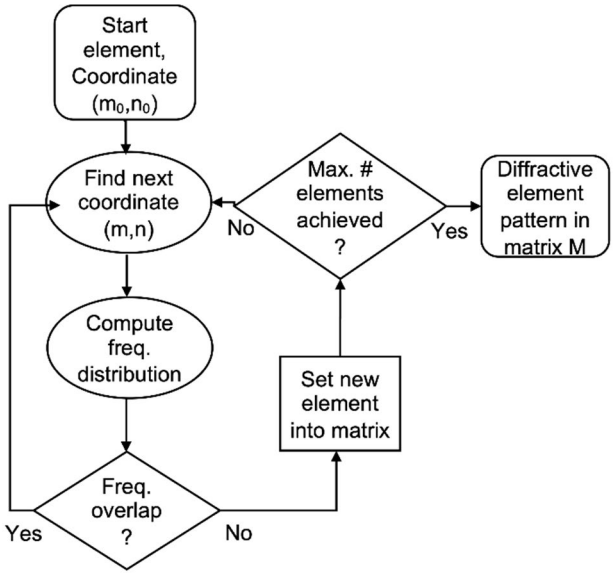

Fig. 4. Algorithmic framework for finding a pattern design.

and described (top round element in flowchart Fig. 4). Parameters such as the element density, number of elements, and the minimum fringe distance are compared for different pattern areas. At the end of the section, we show the measured far-field diffraction patterns for selected designs and their computed spatial frequencies. For comparison, the exemplary designs are shown for circular areas with a diameter of 7 mm and for square areas, with side length of 7 mm. All the diffraction element diameters are 150 μm.

A. Circular Pattern

The circular design follows a deterministic approach. From multipinhole interferometers [2], [12], this design is known. Geometrically, it can be shown (supporting information) that, for a certain diffractive element diameter D_{E} and an odd number of elements N_{o}, the minimum radius r of the circle on which the elements are equidistantly aligned can be calculated using

$$r \geq \frac{D_{\mathrm{E}}}{2 \sin\left(\frac{\pi}{N_o}\right) \sin\left(\frac{\pi}{2N_o}\right)}. \tag{2}$$

Exemplarily the circular pattern for $N_{\mathrm{o}} = 15$ is shown in Fig. 5(a). From the far-field diffraction pattern [see Fig. 5(b)], the spatial frequencies are computed in the Fourier domain [see Fig. 5(c)]. The autocorrelation dc component in the center is filtered out. The inner circle of frequencies results from interference fringes of neighboring diffraction elements. The outer frequency circle results from elements that are on the opposite side of the circle. According to (2), a maximum number of 15 diffraction elements, with a diameter of 150 μm, can be placed on a circle with a diameter of 7 mm.

To observe the dependencies of the design parameters described in (2), the density and number of elements are plotted for different element sizes [see Fig. 5(d)]. For increasing the number of elements, the circle radius has to increase and the element density decreases. The smaller the diameter of the diffraction elements is, the smaller the diameter of the spatial frequencies in the frequency space is. Thus, more elements fit on the circle in the real space without overlapping in the frequency space. For example, when the element diameter on a circle of diameter $d = 9$ mm is reduced by half from 300 to 150 μm, then the number of elements on the circle can be increased from 12 to 17.

B. Golomb Pattern

Golomb rectangles match our requirement of no overlapping spatial frequencies and a high density of diffractive elements.

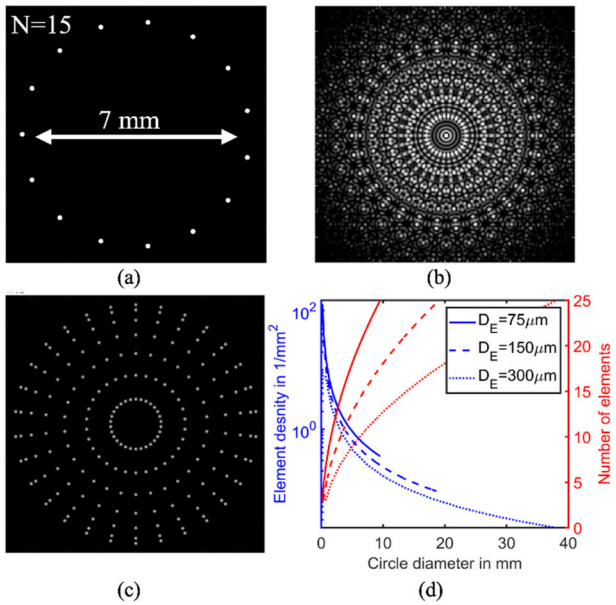

Fig. 5. (a) Circular design with 7-mm diameter. (b) Computed far-field diffraction pattern. (c) Computed spatial frequencies in the Fourier domain. (d) Element density and maximum number of elements relative to the circular pattern diameter for different diffractive element diameters D_E.

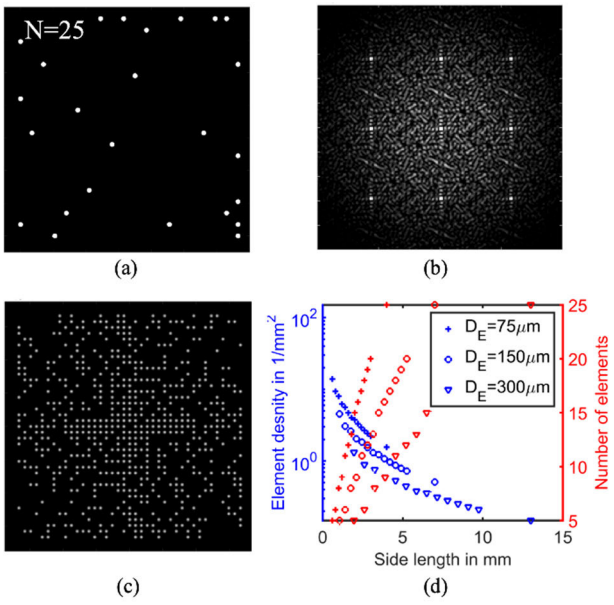

Fig. 6. (a) Optimal Golomb square pattern with a side length of 7 mm. (b) Computed far-field diffraction pattern. (c) Computed spatial frequencies in the Fourier domain. (d) Element density and maximum number of elements relative to the square pattern side length for different diffractive element diameters D_E.

A 20 × 20 optimal Golomb rectangle, introduced by Robinson [28], is transferred into a 7 × 7 mm pattern by choosing column and row spacings of 350 μm. The diameter of the diffractive elements is 150 μm [see Fig. 6(a)]. This pattern achieves the maximum number of elements with $N = 25$. Its density related to its square area is 0.51 elements/mm^2, which is greater than the circle case, with 0.31 elements/mm^2. However, this result changes when a circular reference area for the density calculation is considered. In that case, the circular pattern fills out the space more efficiently. Its density becomes 0.39 elements/mm^2, higher than the Golomb pattern, which has 0.32 elements/mm^2.

Golomb patterns computed by Robinson [28], ranging from 3 × 3 to 25 × 25 Golomb arrays, are transferred into a real-space pattern for microdisk diameters of 75, 150, and 350 μm. The column and row spacings are 200, 350, and 650 μm ($2D_E + 50$ μm). The corresponding element density plot is shown in Fig. 6(d). It has a similar behavior to that of the circular pattern. But the big difference is that the overall density is higher, especially for larger patterns with higher N values, which is explained by the inefficient use of the empty space in a circle and becomes worse for larger circle diameters.

In the following sections, we search for patterns that fill out a circular area more effectively than the circular pattern introduced in Section III-A and which reach similar densities to the optimum Golomb pattern related to a square area.

C. Random Pattern

Another method is to choose the coordinate of the next element randomly within the defined area. In our example [see Fig. 7(a)], the area is circular with a diameter of 7 mm. Since the autocorrelation part in the algorithm is the computationally most expensive one, we introduce a "chromosome" [28],

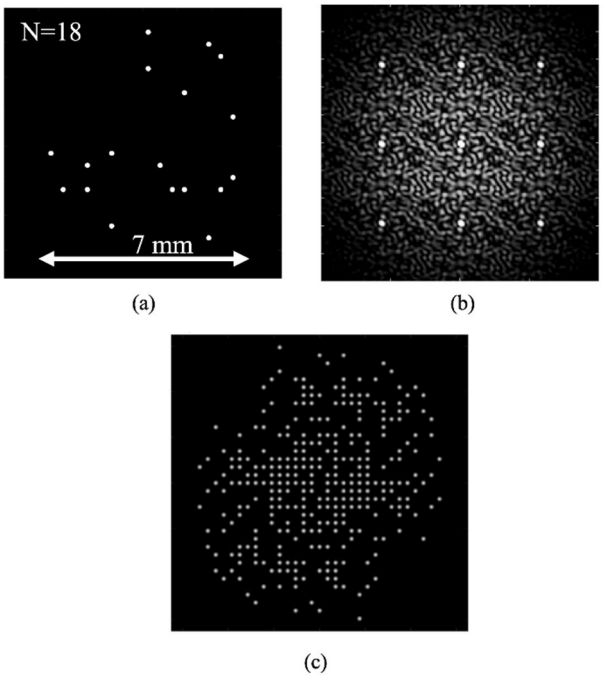

Fig. 7. (a) Random pattern in the circular area of diameter 7 mm. (b) Computed far-field diffraction pattern. (c) Computed spatial frequencies in the Fourier domain.

which contains the information from all existing difference vectors (spatial frequencies) produced by each pair of two existing elements.

The chromosome is an array for which the center is defined as the zero-difference vector [see Fig. 8(b)]. Each marked position in the matrix stands for one difference vector that exists in the element matrix [see Fig. 8(a)]. When the chromosome matrix is overlaid onto the existing element matrix, the middle (zero position) of the chromosome matrix

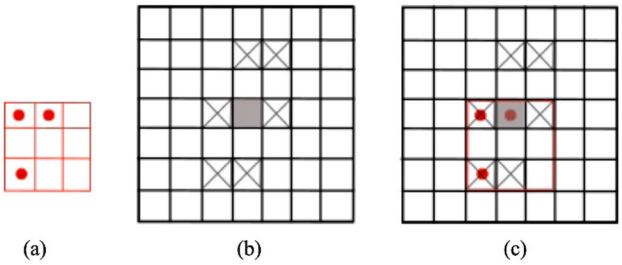

Fig. 8. Illustration of the chromosome. (a) Test matrix with three existing elements. (b) Corresponding chromosome matrix. (c) Chromosome overlapped with matrix element ($m = 1$ and $n = 2$).

TABLE I
COMPUTATIONAL RESOURCES FOR 7 mm RANDOM PATTERNS WITH $N = 18$

	w. chrom.	w.o. chrom.	R.S. FFT
Time	57 ms	97 ms	58 s
Autocorr. Calls	19	57	-
Used Memory	3 KB	3 KB	33 GB

Average values based on n=100 pattern designs. W. chrom.: with chromosome, w.o. chrom.: without chromosome, R.S. FFT: real space pattern and its far field and frequency space FFT computation. Available RAM: 261.851 GB, Processor: AMD EPYC 7402P 24-Core, 2800 MHz.

is aligned with each existing element position, and shows the positions that would produce overlapping if they were occupied. This check is much faster than calculating the 2-D autocorrelation, and it is therefore used to rule out potential positions that would certainly result in overlap. Table I shows the computational resources used for the 7-mm random design with 18 elements. The results from the algorithm with and without the chromosome method are compared and also the computation parameters for the far-field intensity distribution and the spatial frequencies of the real-space pattern are shown. Each quantity is the average value of 100 pattern designs. The computation is reduced by half when the chromosome is used. Without the chromosome, the autocorrelation function is called approximately three times more than with the chromosome. The table also shows the benefit of the array approach versus the FFT computation during the search for a pattern. Each spatial frequency computation round would last 58 s on average. Therefore, the whole pattern design would run between 20 and 57 min with and without the chromosome approach, respectively. The chromosome approach is used for all other nondeterministic design approaches too. For a 7-mm diameter circle the maximum number of elements is found, after various trials, to be $N = 18$. The pattern, therefore, has an element density of 0.37 elements/mm^2 for a circular reference area. Compared to the circle, this density represents an improvement of 21%, and the inner space is used much more efficiently than in the case of the circular pattern. Even though the real-space diffraction elements appear to be ordered chaotically, in the Fourier domain the low spatial frequencies are arranged on a grid-like array, which explains the improved results.

D. Spiral Pattern

The spiral design follows an inverse deterministic design approach that starts in the Fourier domain by designing spatial frequencies (difference vectors) positioned on multiple concentric circles [see Fig. 9(a)]. The inner circle has a radius r_0, the radius of the outer spatial frequency circle r_1 depends on the inner radius r_0, and the diameter d_{DE} of the diffractive element. The dependence is derived from the requirement of there being no overlapping spatial frequencies

$$r_{\max} = 2r_0 \tag{3}$$

$$r_1 = r_0 + 2d_{\mathrm{DE}} \tag{4}$$

$$r_n = r_0 + 2nd_{\mathrm{DE}}, \quad n \in \mathbb{N}, \ n \geq 2. \tag{5}$$

Such a design is shown in Fig. 9(a) for a diffractive element diameter of 150 μm and inner radius of $r_0 = 750$ μm. The spatial frequencies always occur in pairs, with the same magnitude but opposite signs (Fig. 9(a) and (b): dotted and solid arrows and circles of the same color). Subsequently, the real-space pattern is set up by summing the difference vectors. Each difference vector starts at a diffractive element and ends at the following one. Therefore, each difference vector adds a new element to the spiral. The spiral starts with the inner circle of lower frequencies marked with the red dotted circle and arrow. Successively, neighboring frequencies (difference vectors) are added to the spiral pattern. After placing the last difference vector before the opposite of the starting frequency is reached (red circle marked frequency), the frequency selection jumps to the outer circle (green difference vector) and successfully adds the frequencies of the outer circle until the opposite frequency of the starting outer frequency is reached (green dotted circle). This results in two connected half circles [see Fig. 8(b)]. Fig. 8(c) shows the far-field diffraction pattern. From the computed spatial frequencies [see Fig. 9(d)], it can be seen that this design only guarantees that there is no overlap of the frequencies on the designed circles. Higher frequencies that are produced by nonneighboring elements are ignored.

The spiral pattern can be reassembled as a rectangular-shaped array [see Fig. 9(e)]. Therefore, each pair of diffractive elements is placed on a grid point in an array. The distance between the grid lines is at least twice the maximum difference vector length used in the spiral design. In Fig. 8(f), the spatial frequencies are shown. Not all of the element combinations fit on the predefined area of 7×7 mm. The circular spiral pattern has a density of 0.47 elements/mm^2, which is an improvement of 21%. The array-shaped pattern has a circular area density of 0.23 elements/mm^2. The density of both patterns related to a rectangular area is 0.37 elements/mm^2.

E. Concentric Circles Pattern

The concentric circle design follows a deterministic inverse design approach, in a similar fashion to that for a spiral pattern. Again, two spatial frequency circles are designed in the Fourier domain. In contrast, the goal is to produce in real space not half circles but concentric full circles. Therefore, only every second frequency (difference vector) on one circle is chosen but, in contrast to the spiral case, a full-frequency

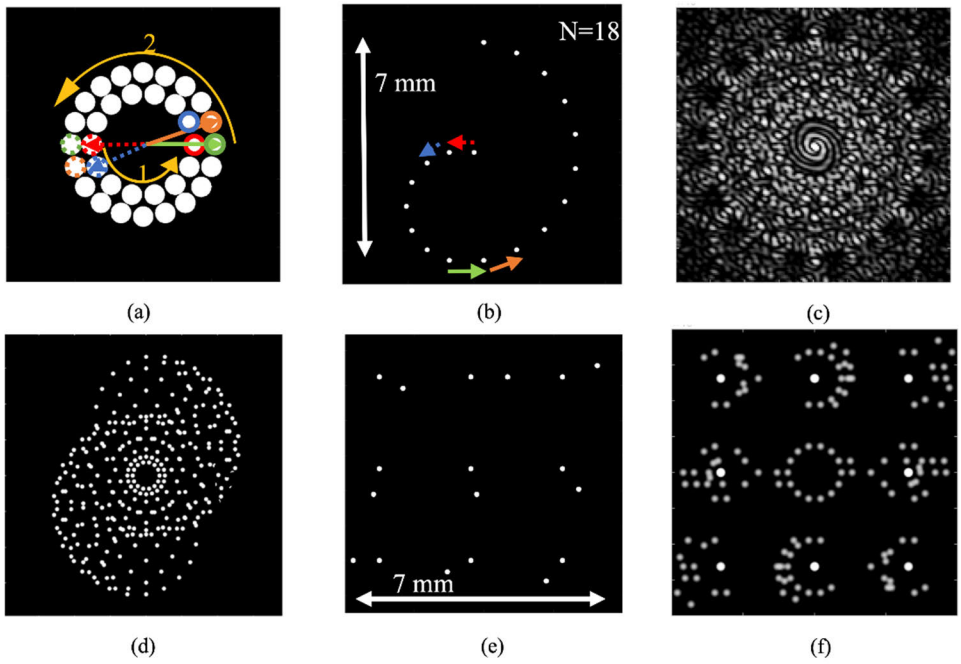

Fig. 9. Spiral pattern design. (a) Design of spatial frequencies in Fourier domain. (b) Transfer of design from Fourier domain into real space. (c) Computed far-field diffraction pattern. (d) Computed spatial frequencies in the Fourier domain. (e) Element array made out of pairs from spiral design. (f) Computed spatial frequencies in the Fourier domain (inner region).

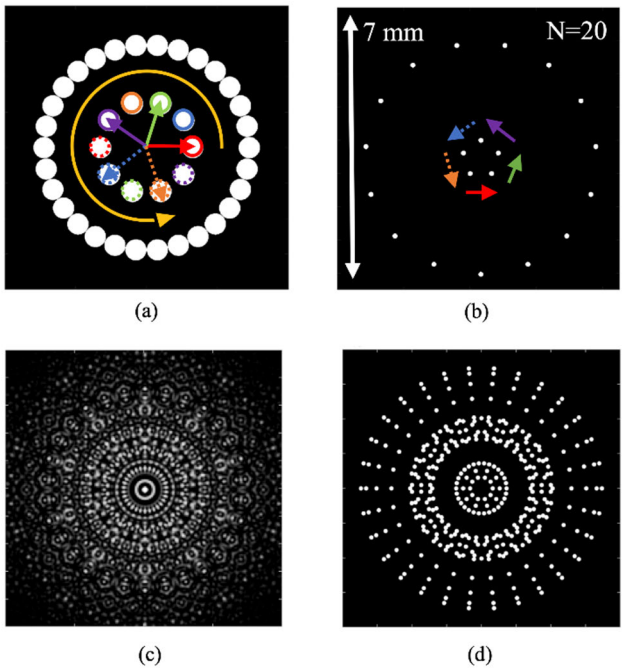

Fig. 10. (a) Designed spatial frequency circles in the Fourier domain. (b) Concentric circular pattern design of diameter 7 mm. (c) Computed far-field diffraction pattern. (d) Computed spatial frequencies in the Fourier domain.

circle is completed [see Fig. 10(a)]. Once this has been carried out, the outer frequency circle is started in the same way. Each frequency circle produces one closed circle of diffractive elements in real space. The circles in real space are aligned concentrically. Fig. 10(c) shows the resulting far-field diffraction pattern and Fig. 10(d) shows the corresponding spatial frequencies in the Fourier domain.

The inner (low) frequency circle is chosen to be small enough not to produce difference vectors of nonneighboring inner circle elements that overlap with the spatial frequencies of the outer frequency circle. This design guarantees the nonoverlapping frequencies of all combinations produced by the inner frequency circle but produces some spatial frequencies that are very close to each other. Neighboring elements on the outer circle and element pairs with more than two elements between them show a larger interfrequency spacing again.

F. Archimedes Smart Array Pattern

The Archimedes smart array pattern is designed on the basis of the algorithm described in Fig. 3 and the chromosome (see Fig. 11). To check the uniqueness of the spatial frequencies, the faster alternative procedure described in Section II-D was used. The area was therefore divided into a 20 × 20 array [see Fig. 11(a)]. To find the next coordinate, the algorithm was moved along an Archimedes spiral path from the outside to the inside of the array and selected the matrix element in which the spiral coordinate was located. Fig. 11(a) shows the selected matrix element in yellow for the first half-turn. The movement from outside to inside was chosen since, on the outside, the largest number of elements was expected, in a Golomb array [28]. The Archimedes spiral was designed on the basis of polar coordinates with radius r and angle α

$$c = g/2\pi \tag{6}$$

$$r = c\alpha. \tag{7}$$

The gap g between the spiral lines was the same as the matrix element size. To transfer the geometry to the real-space pattern, the matrix element size was defined to be 350 μm, and its diameter was 7 mm. The Cartesian coordinates were calculated using

$$x = r\cos\alpha \tag{8}$$

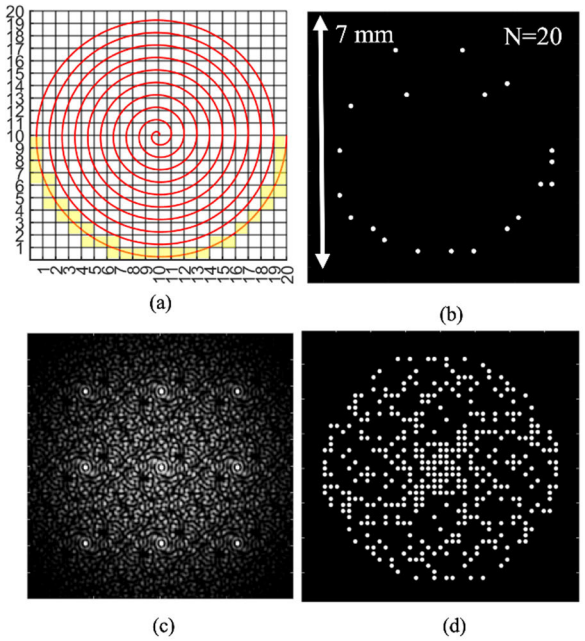

Fig. 11. (a) Archimedes spiral plotted on grid lines. The grid lines show the 20×20 array. The yellow marked cells show the sequence of selected array cells during the first half round. (b) Archimedes smart array pattern design of diameter 7 mm. (c) Computed far-field diffraction pattern. (d) Computed spatial frequencies in the Fourier domain.

$$y = r \sin \alpha. \tag{9}$$

G. Comparison Based on Different Area Sizes

To compare different designs, we have looked at their element density (elements/mm^2), number of elements, and their minimum fringe distance in the far-field, for a focal length of $f = 125$ mm. Since the achievable density drops with increasing area size, different area sizes and shapes are considered. Fig. 12 shows, for the different designs, the element density for circular areas (blue) and square-shaped areas (orange). The different circular areas have diameters d of 4, 5.7, 7, and 9.9 mm. The square areas have the same number, but instead of the diameter, the numbers represent the side length a of the square. Furthermore, the total number of elements and the minimum fringe distance is plotted [see Fig. 12(b)]. As a lower benchmark for the element density, the density of the circular pattern is used (blue dotted line), and as an upper limit, the Golomb pattern density for a square area is used (orange dotted line). Both show that, with increasing area, the achievable element density drops.

Starting with an area of dimension $r = 4$ mm ($a = 4$ mm), it can be seen that the density of the Golomb pattern is about 21% higher when, in both cases, the optimum reference area is used (for the circle pattern a circular one and for the Golomb pattern a square). Considering the Gaussian laser beam in our experimental setup, it also makes sense to use a circular area for the Golomb pattern as a reference area. However, in this case, the density of the square Golomb pattern is about 29% lower than that of the circular pattern. The question becomes how to increase the element density for circular areas to get closer to the limit of the Golomb pattern for square areas.

Both the random and the Archimedes spiral smart arrays are, with densities of 1.03 elements/mm^2, very close to the Golomb limit of 1.06 elements/mm^2. Their number of total elements is still smaller but the circle has a smaller area than the square from the Golomb pattern.

For better comparison with the previous designs of square areas with side dimension $a = 4$ mm, circular areas of diameter 5.7 mm ($4 \text{ mm} \times \sqrt{2}$) follow. This diameter gives the circular area that would be illuminated with a Gaussian beam when seeking to illuminate a square area with side length $a = 4$ mm. It can be seen that the density of the Golomb pattern with the 4-mm design (and referenced to a circular area) is still greater if the 5.7-mm circular pattern design was used, which fills out the edges of the light spot better. However, the Archimedes spiral pattern achieves the same circular reference area density and the concentric circle (+5%) design beat the 4-mm square Golomb pattern when used with the same circular reference area. It achieves to include one element more within the circular area than the Golomb pattern in the smaller square area. It can also be shown that the Archimedes spiral smart array design performs better when starting from the outside and moving to the inside during design (OI), as compared with moving from the inside to the outside (IO).

Next, designs with an area based on diameters and side length of 7 mm are investigated. The number of elements increases for these designs. Again, the square Golomb pattern, with 25 elements, has an element density that is about 31% higher compared to the circular pattern density (for optimum reference areas in each case) but when also using a circular reference area for the square Golomb pattern, the density drops by about 18% compared with the circular design. As before, the question is how to achieve an element density for circular reference areas close to the Golomb limit of 0.51 elements/mm^2.

With multiple runs of the random approach, we obtain a 20% improvement compared with the circular pattern benchmark. Furthermore, the spiral pattern shows an improvement of 20%, but it is still about 8% lower than the Golomb limit. The concentric circle design surpasses the limit with a density of 0.52 elements/mm^2. However, it is not equal to the square Golomb pattern, since some pairs of nonneighbor elements result in frequencies with a very low interfrequency spacing and partial overlapping.

The Archimedes spiral-based smart array has an element density of 0.52 elements/mm^2, too. It surpasses the square Golomb limit and possesses only unique spatial frequencies. A pattern that has the same density as an equivalent square Golomb pattern has therefore been achieved, but it is optimized for circular-shaped Gaussian beams. The Golomb pattern has still five more elements but this is due to its higher square area.

If the 7-mm Golomb square area would be illuminated with a Gaussian beam, a 9.9-mm diameter ($7 \text{ mm} \times \sqrt{2}$) circular design would be beneficial. The Archimedes design is again the highest-density design. Surpassing the benchmark by about 36% and even the 7-mm square Golomb array by about 13%, when a circular reference area is used (as is the case for

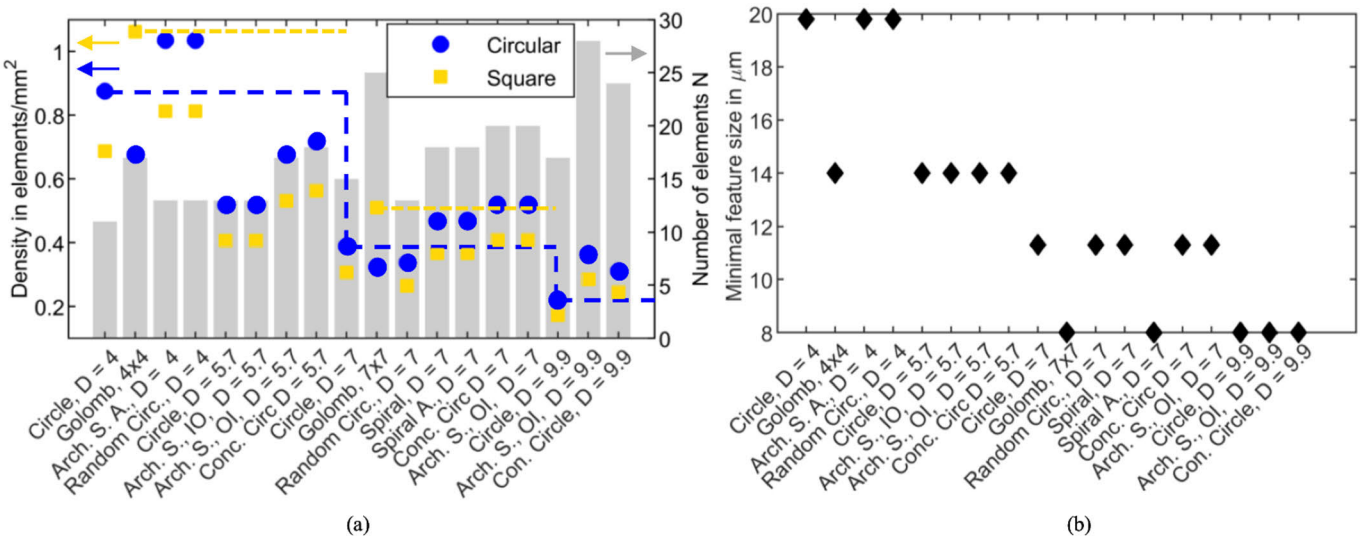

Fig. 12. (a) Element density and number of elements, and (b) minimal fringe distance s (feature size) of various pattern designs for different area sizes and shapes. Abbreviations: Arch. S. A.: Archimedes smart array, IO: In to out, OI: Out to in, Conc. Circ: Concentric circle, and Spiral A.: Spiral Array.

Gaussian beams). This can be attributed to three additional elements that can be placed within the circular area enclosing the 7×7-mm^2 square area.

In Fig. 12(b), the minimum fringe distance within the patterns is plotted. It is determined by the maximum element distance in the pattern. Therefore, a decrease in the minimum feature size for an increase in pattern diameter is observed. It is an important value, as there should be at least two camera pixels available to resolve the spatial frequency. Depending on the camera chip, this sets a limit to the maximum distance between elements. On the other hand, in such patterns, the high frequencies with small feature sizes could be ignored and one could rely on element pairs of closer distance only.

H. Experimental Characteristics of Selected Patterns

For experimental validation, the circular [see Fig. 13(a) and (b)] and Archimedes spiral [see Fig. 13(c) and (d)] designs were fabricated. All patterns were designed in the 4-mm geometry. The diffractive elements were fabricated by micro-structuring a photonic crystal slab [11]. A laser common path interferometric setup [11] was used to excite the highly reflective GMR in the microdisks and to measure, in reflection (see Fig. 1), their near-field [see Fig. 13(b) and (d)] and far-field diffraction patterns [see Fig. 13(f) and (h)]. From the measured far-field intensity, the magnitude of the spatial frequencies in the Fourier Domain was computed via the 2D-FFT [see Fig. 13(j) and (l)]. As a reference, the images on the left of the experimental images show the theoretical patterns computed with MATLAB, as described in Fig. 2.

Experimentally, not all the diffractive elements reflected the same intensity, due to slightly different elementary resonances [30]. Some of the spatial frequencies, therefore, had better visibility than others. But overall the agreement was very high and even the details of the far-field diffraction patterns can be seen, when Fig. 13(e) is compared with Fig. 13(f) and (g) is compared with Fig. 13(h). To compare the measured spatial frequencies of the circular pattern with the calculated ones, the spatial frequencies along the blue marked intersection [see Fig. 13(i)] are plotted in Fig. 14(a) and it can be seen that, in theory, five frequency pairs are aligned around the zero autocorrelation part in the center. In the computed frequency pattern image, the autocorrelation part in the center is filtered out—but, for the plot of the intersection, it is considered. The highest frequency pair $(f5, -f5)$ of the measured pattern was used to scale the measured intersection plot to the size of the computed intersection. It can be seen that all the frequencies that are computed are present in the measured magnitude signal, and their relative spacing and positioning match with the computed spatial frequencies. The same can be said about the intersection taken from the Archimedes spiral spatial frequency pattern. In contrast to earlier, the intersection does not cross the center—which makes it possible to observe nine different spatial frequencies, $f1$–$f9$. After scaling, it can be seen that the number and the positions of the spatial frequencies match very well with the theory.

One difference can be seen in the frequency signal of the circular pattern. The autocorrelation part in the center is much broader than expected from theory, which is a measurement error that arises from light reflected at the glass–air interface on the backside of the glass substrate that supports the microdisks. The reflected light is a planar wavefront that is focused by the Fourier lens into the middle of the back focal plane where the camera is located. A similar effect is seen in Fig. 13(l). As proof, the theoretical computed far-field intensity pattern from Fig. 13(g) is manipulated. An artificially bright spot is placed in the center of the far-field intensity frame [see Fig. 15(a)] to simulate the focused planar wavefront. Its Fourier transform with the spatial frequencies in Fig. 15(b) shows the same effect as in the measurement. A similar deviation from theory is the background in the Fourier domain image of the measured far fields. This background looks like "clouds" in the image, Fig. 13(j) and (l). However, from the

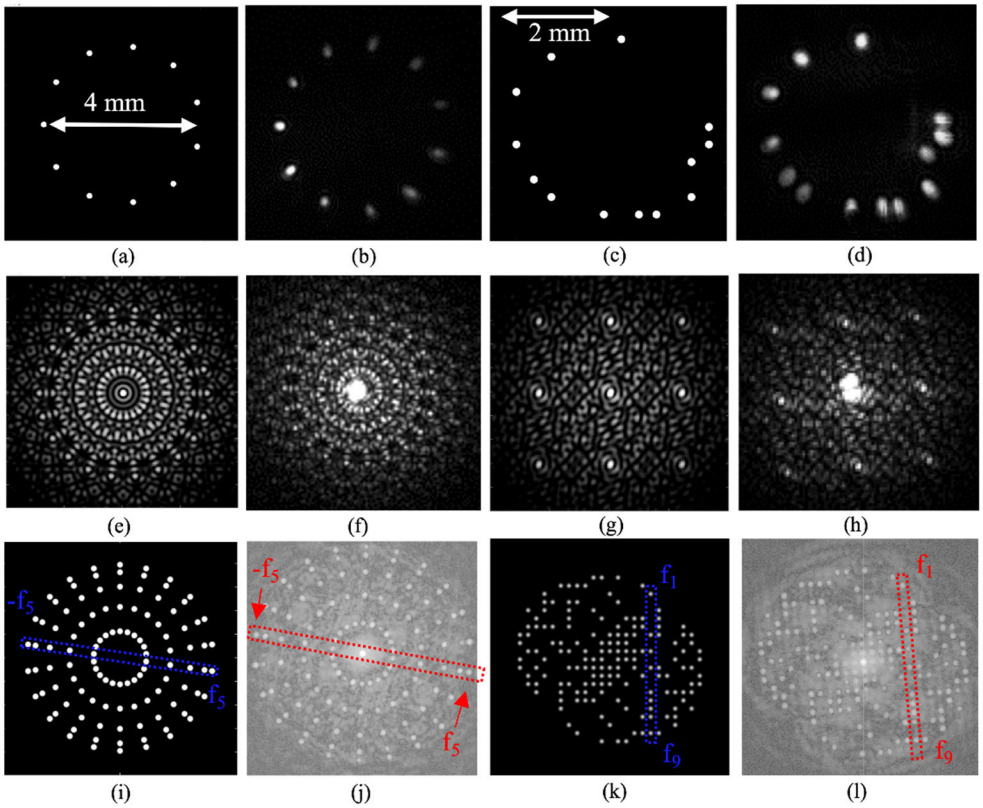

Fig. 13. Comparison between experimental results and designs. (a) Circular pattern design and (b) its measured near field reflection. (c) Archimedes pattern design and (d) its measured near field reflection. (e) Computed far-field from circular design and (f) its measured far-field. (g) Computed far-field from Archimedes spiral design and (h) its measured far-field. (i) Fourier transform of the computed circular pattern far-field. (j) Computed far-field from measured circular far-field showing spatial frequencies. The blue and red rectangles show the frequency selection plotted in Fig. 14(a). (k) Fourier transform of the computed Archimedes pattern far-field. (l) Computed far-field from measured Archimedes far-field showing spatial frequencies. The red rectangle shows the frequency selection plotted in Fig. 14(b).

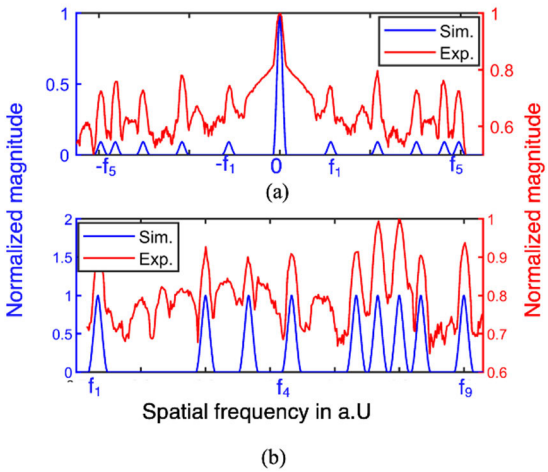

Fig. 14. Comparison of spatial frequency magnitudes between simulation (blue) and measurement (red). The spatial frequencies of (a) circular and (b) Archimedes spiral patterns are selected from the areas marked with the dotted line in Fig. 13.

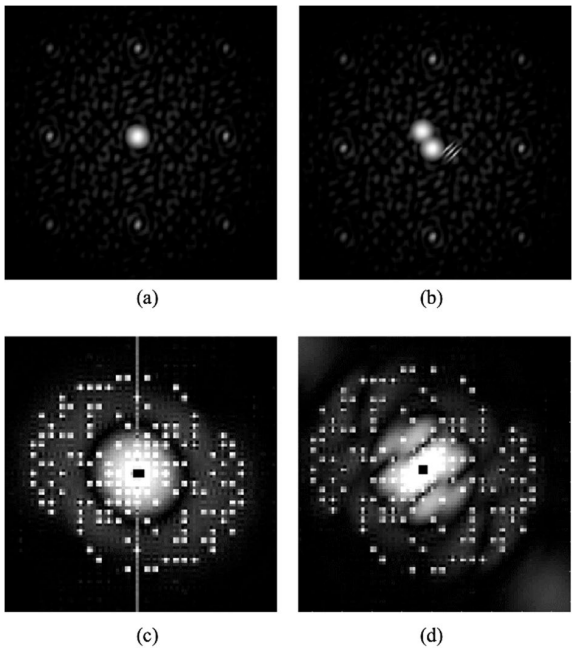

Fig. 15. (a) and (b) Manipulated theoretical far field intensity images based on Fig. 13(g) with optical signals of disturbances and (c) and resulting spatial frequencies in the Fourier domain for (a) and (d) for (b).

intersection plots, it can be seen that the spatial frequencies that are more dominant can still be located. During phase measurement, the difference between multiple frames is observed. In the case of a constant "frequency cloud" background, this difference is subtracted from the phase shift signal. The cloudiness is explained by the two bright spots and a small interference pattern in the middle of the far-field intensity image [see Fig. 13(h)] that should not exist in theory [see Fig. 13(g)]. The origin of the center spot was explained before, the second one originates probably from a tilted planer war

front reflected at another interface that is slightly tilted relative to the first one. This effect is also simulated. The manipulated theoretical far-field intensity pattern from Fig. 13(g) is shown in Fig. 15(b) and its spatial frequencies in the Fourier domain in Fig. 15(d). This shows that as in the experiments the clouds can be observed in the theoretical computed frequency distribution too, when the optical signals of disturbance are included.

IV. Conclusion

Multiplex common-path interferometric sensors based on the combined measurement of overlapping interference patterns with nonoverlapping spatial frequencies require that there is a unique set of spatial frequencies. We have shown that the circular pattern common in multipinhole interferometry has a low sensor element/pinhole density. From other sensing technologies, such as sonar and radar, Golomb rectangles are known and provide element patterns with the maximum density. For the introduced pattern designs with a diameter of 7 mm, the Golomb pattern has a 31% higher density than the circular pattern. However, they are so far available only for rectangular areas.

We have investigated several different design approaches and patterns with the aim of increasing the element density for circular-shaped patterns, with the goal of achieving element densities close to those for the Golomb rectangle. Thereby, the pattern computation time was reduced by about four orders of magnitude from minutes to milliseconds, by employing a reduced array representation of the diffraction elements. In addition, the "chromosome method" doubled the speed of computation.

We have shown that an Archimedes spiral design fulfills this requirement of nonoverlapping spatial frequencies, combined with densities similar to the Golomb rectangle. For the 7-mm design, its density is 0.52 elements/mm^2 slightly higher than the rectangular Golomb pattern density with a square area density of 0.51 elements/mm^2. Furthermore, concentric circular designs are a good choice when there is reliance on interference between neighboring and far-distance element pairs only. For the larger 9.9 mm design, the Archimedes spiral has a 36% higher density compared to its circular benchmark and a 13% higher density compared to the 7-mm square Golomb pattern illuminated with a Gaussian beam with a diameter of 9.9 mm (circular reference area). To increase the number of diffraction elements, beyond the amount of the optimized patterns, larger pattern areas are required. However, it has been shown that the element density drops with increasing area of measurement. Different geometry sizes relevant to our common path interferometric measurement setup were therefore investigated.

To validate the theoretical pattern designs two different patterns in the 4-mm geometry were fabricated and optically characterized. Their far-field diffraction pattern and 2D-FFT show the spatial frequency distribution match well with the theoretical computed patterns. The difference in the background signal, observed as "clouds," is attributed to reflections in the setup disturbing the signal.

The investigated pattern design allows for an increase in the sensor density and hence the multiplex ability of multipinhole and multimicrodisk interferometers. Besides, the pattern might be used in quantum information processing systems. For sensor systems with element numbers $N \gg 25$, we recommend combining multiple smaller patterns ($N < 15$) and multiplexing by separating the patterns and optical output spatially. Another alternative is to place multiple patterns next to each other, each pattern being based on elements with different resonance wavelengths. With a broader excitation spectrum, only elements of the same pattern would interfere with each other, since elements from other patterns would reflect a different wavelength. In the case of nonresonant diffraction elements, the different wavelengths must be separated spatially.

Instead of photonic crystal microdisk diffraction elements, optical fiber outputs could be arranged with the proposed pattern and imaged with a camera CMOS sensor without the need of separating the outputs or using multiple photodiodes.

Recently, the inverse design method for nanophotonic structures was proposed [31], [32], [33]. This would be an interesting approach to find alternative circular pattern arrangements. However, at least for square-shaped patterns the maximum element density is achieved with the Golomb pattern design already.

References

[1] D. Zhao, J. Zhang, P. Yao, X. Jiang, and X. Chen, "Photonic crystal Mach–Zehnder interferometer based on self-collimation," *Appl. Phys. Lett.*, vol. 90, no. 23, Jun. 2007, Art. no. 231114, doi: 10.1063/1.2746942.

[2] M. S. Murib, D. Martens, and P. Bienstman, "Label-free real-time optical monitoring of DNA hybridization using SiN Mach–Zehnder interferometer-based integrated biosensing platform," *J. Biomed. Opt.*, vol. 23, no. 12, pp. 1–7, Dec. 2018, doi: 10.1117/1.jbo.23.12.127002.

[3] M. Yadav and A. Aksnes, "Multiplexed Mach–Zehnder interferometer assisted ring resonator sensor," *Opt. Exp.*, vol. 30, no. 2, pp. 1388–1396, 2022, doi: 10.1364/oe.448023.

[4] W. R. Wong and P. Berini, "Integrated multichannel Young's interferometer sensor based on long-range surface plasmon waveguides," *Opt. Exp.*, vol. 27, no. 18, pp. 25470–25484, 2019, doi: 10.1364/oe.27.025470.

[5] X. Guan, X. Wang, and L. H. Frandsen, "Optical temperature sensor with enhanced sensitivity by employing hybrid waveguides in a silicon Mach–Zehnder interferometer," *Opt. Exp.*, vol. 24, no. 15, pp. 16349–16356, 2016, doi: 10.1364/oe.24.016349.

[6] N. A. Ushakov, A. A. Markvart, G. S. Member, and L. B. Liokumovich, "Multiplexed fiber optic Fabry–Pérot interferometric sensors," *IEEE Sensors J.*, vol. 20, no. 19, pp. 11302–11312, May 2020.

[7] X.-G. Li, Y. Zhao, L. Cai, and X. Zhou, "Measurement of magnetic field and temperature based on fiber-optic composite interferometer," *IEEE Trans. Instrum. Meas.*, vol. 66, no. 7, pp. 1906–1911, Jul. 2017, doi: 10.1109/TIM.2017.2670067.

[8] P. Niewczas et al., "Interrogation of extrinsic Fabry–Pérot interferometric sensors using arrayed waveguide grating devices," *IEEE Trans. Instrum. Meas.*, vol. 52, no. 4, pp. 1092–1096, Aug. 2003, doi: 10.1109/TIM.2003.814828.

[9] P. L. Swart, A. A. Chtcherbakov, and A. J. V. Wyk, "Multiplexed fibre Bragg grating Fabry–Pérot interferometers for measuring the coefficients of thermal expansion of anisotropic solids," *Meas. Sci. Technol.*, vol. 17, no. 5, pp. 1146–1151, May 2006, doi: 10.1088/0957-0233/17/5/S35.

[10] Q. Wang, B.-T. Wang, L.-X. Kong, and Y. Zhao, "Comparative analyses of bi-tapered fiber Mach–Zehnder interferometer for refractive index sensing," *IEEE Trans. Instrum. Meas.*, vol. 66, no. 9, pp. 2483–2489, Sep. 2017, doi: 10.1109/TIM.2017.2707962.

[11] F. Chen, Y. Jiang, L. Zhang, L. Jiang, and S. Wang, "Fiber optic refractive index and magnetic field sensors based on microhole-induced inline Mach–Zehnder interferometers," *Meas. Sci. Technol.*, vol. 29, no. 4, Feb. 2018, Art. no. 045103, doi: 10.1088/1361-6501/aa902c.

[12] X. Bao, "Prospects on ultrasound measurement techniques with optical fibers," *Meas. Sci. Technol.*, vol. 34, no. 5, May 2023, Art. no. 051001, doi: 10.1088/1361-6501/acb5b2.

[13] P. K. Sahoo, S. Sarkar, and J. Joseph, "High sensitivity guided-mode-resonance optical sensor employing phase detection," *Sci. Rep.*, vol. 7, no. 1, p. 7607, Aug. 2017, doi: 10.1038/s41598-017-07843-z.

[14] I. Barth, D. Conteduca, C. Reardon, S. Johnson, and T. F. Krauss, "Common-path interferometric label-free protein sensing with resonant dielectric nanostructures," *Light, Sci. Appl.*, vol. 9, no. 1, p. 96, Jun. 2020, doi: 10.1038/s41377-020-0336-6.

[15] L. Laplatine et al., "Silicon photonic olfactory sensor based on an array of 64 biofunctionalized Mach–Zehnder interferometers," *Opt. Exp.*, vol. 30, no. 19, pp. 33955–33968, 2022, doi: 10.1364/oe.461858.

[16] P. Klapetek et al., "Multiple-fibre interferometry setup for probe sample interaction measurements in atomic force microscopy," *Meas. Sci. Technol.*, vol. 31, no. 9, Sep. 2020, Art. no. 094001, doi: 10.1088/1361-6501/ab85d8.

[17] T. V. Reichold, P. D. Ruiz, and J. M. Huntley, "Nine-hundred-channel single-shot surface roughness measurement using hyperspectral interferometry," *Meas. Sci. Technol.*, vol. 31, no. 4, Apr. 2020, Art. no. 045014, doi: 10.1088/1361-6501/ab5e98.

[18] J. Bläsi and M. Gerken, "Multiplex optical biosensors based on multi-pinhole interferometry," *Biomed. Opt. Exp.*, vol. 12, no. 7, pp. 4265–4275, Jul. 2021, doi: 10.1364/BOE.426991.

[19] G. X. Wei, Y. Y. Liu, S. G. Fu, and P. Wang, "Measurement of fractional optical vortex by a ring-type multi-pinhole interferometer," *Adv. Mater. Res.*, vols. 433–440, pp. 6339–6344, Jan. 2012, doi: 10.4028/www.scientific.net/AMR.433-440.6339.

[20] C.-S. Guo, S.-J. Yue, and G.-X. Wei, "Measuring the orbital angular momentum of optical vortices using a multipinhole plate," *Appl. Phys. Lett.*, vol. 94, no. 23, Jun. 2009, Art. no. 231104, doi: 10.1063/1.3151920.

[21] G. C. G. Berkhout and M. W. Beijersbergen, "Method for probing the orbital angular momentum of optical vortices in electromagnetic waves from astronomical objects," *Phys. Rev. Lett.*, vol. 101, no. 10, Sep. 2008, Art. no. 100801, doi: 10.1103/PhysRevLett.101.100801.

[22] G. C. Berkhout and M. W. Beijersbergen, "Measuring optical vortices in a speckle pattern using a multi-pinhole interferometer," *Opt. Exp.*, vol. 18, no. 13, pp. 13836–13841, 2010, doi: 10.1364/oe.18.013836.

[23] J. Bläsi, M. Köpke, and M. Gerken, "Noise reduced multi-pinhole interferometry based on resonant pindisks," in *Proc. OSA Opt. Sensors Sens. Congr.*, 2021, pp. 8–9, doi: 10.1364/fts.2021.fw3d.2.

[24] M. R. Dennis and J. B. Götte, "Topological aberration of optical vortex beams: Determining dielectric interfaces by optical singularity shifts," *Phys. Rev. Lett.*, vol. 109, no. 18, pp. 1018–1020, Oct. 2012, doi: 10.1103/PhysRevLett.109.183903.

[25] S. Golomb and H. Taylor, "Two-dimensional synchronization patterns for minimum ambiguity," *IEEE Trans. Inf. Theory*, vol. IT-28, no. 4, pp. 600–604, Jul. 1982, doi: 10.1109/TIT.1982.1056526.

[26] J. Robinson, "Golomb rectangles," *IEEE Trans. Inf. Theory*, vol. 31, no. 6, pp. 781–787, Nov. IT-1985, doi: 10.1109/TIT.1985.1057108.

[27] J. P. Robinson, "Golomb rectangles as folded rulers," *IEEE Trans. Inf. Theory*, vol. 43, no. 1, pp. 290–293, Jan. 1997, doi: 10.1109/18.567715.

[28] J. P. Robinson, "Genetic search for Golomb arrays," *IEEE Trans. Inf. Theory*, vol. 46, no. 3, pp. 1170–1173, May 2000, doi: 10.1109/18.841202.

[29] D. Curic, L. Giner, and J. S. Lundeen, "High-dimension experimental tomography of a path-encoded photon quantum state," *Photon. Res.*, vol. 7, no. 7, pp. A27–A35, 2019, doi: 10.1364/prj.7.000a27.

[30] J. Bläsi and M. Gerken, "Multiplex microdisk biosensor based on simultaneous intensity and phase detection," *Opt. Exp.*, vol. 31, no. 3, pp. 4319–4333, Jan. 2023, doi: 10.1364/OE.477258.

[31] M. Burger, S. J. Osher, and E. Yablonovitch, "Inverse problem techniques for the design of photonic crystals," *IEICE Trans. Electron.*, vol. E87C, no. 3, pp. 258–265, 2004.

[32] S. Molesky, Z. Lin, A. Y. Piggott, W. Jin, J. Vucković, and A. W. Rodriguez, "Inverse design in nanophotonics," *Nature Photon.*, vol. 12, no. 11, pp. 659–670, Nov. 2018, doi: 10.1038/s41566-018-0246-9.

[33] L. Su, D. Vercruysse, J. Skarda, N. V. Sapra, J. A. Petykiewicz, and J. Vuckovic, "Nanophotonic inverse design with SPINS: Software architecture and practical considerations," 2019, *arXiv:1910.04829*.

Johannes Bläsi received the B.S. degree in electrical and information engineering from Ulm University, Ulm, Germany, in 2014, and the M.S. degree in optics and photonics from the Karlsruhe School of Optics and Photonics (KSOP), Karlsruhe Institute of Technology, Karlsruhe, Germany, in 2017. He is currently pursuing the Ph.D. degree in electrical engineering with the University of Kiel, Kiel, Germany.

His research interests include photonic crystal-based optical biosensors and nanophotonics.

Richard De La Rue (Life Fellow, IEEE) joined Glasgow University, Glasgow, U.K., in 1971, as a Lecturer, and he became a Senior Lecturer in 1982, a Reader in 1985, and a Professor of optoelectronics in 1986. He currently has the status of Honorary Professor. His research has focused on photonic-crystal and photonic-wire structures, waveguide microcavities, and metamaterials. His research on photonic crystals has evolved to cover compact lasers, planar microcavities, photonic-crystal structured LEDs, and synthetic and inverse opal structures. His research on metamaterials has particularly emphasized the use of semiconductor substrates and the impact of the choice of metallization. More recently he has been involved in research on the photonic properties of graphene oxide.

Martina Gerken (Senior Member, IEEE) received the Dipl.-Ing. degree in electrical engineering from the University of Karlsruhe, Karlsruhe, Germany, in 1998, and the Ph.D. degree in electrical engineering from Stanford University, Stanford, CA, USA, in 2003.

From 2003 to 2008, she was an Assistant Professor with the University of Karlsruhe. In 2008, she was appointed as a Full Professor of electrical engineering and the Head of the Chair for Integrated Systems and Photonics, Kiel University, Kiel, Germany.